Sunflower: Locating Underwater Robots From the Air

Charles J. Carver[†], Qijia Shao[†], Samuel Lensgraf, Amy Sniffen, Maxine Perroni-Scharf,
Hunter Gallant, Alberto Quattrini Li, and Xia Zhou

{ccarver.gr, qijia.shao.gr, samuel.e.lensgraf.gr, amy.k.sniffen.gr, maxine.a.perroni-scharf.21, hunter.j.gallant.gr}@dartmouth.edu
{alberto.quattrini.li, xia.zhou}@dartmouth.edu
Department of Computer Science, Dartmouth College, [†] Co-primary Authors

ABSTRACT

Locating underwater robots is fundamental for enabling important underwater applications. The current mainstream method requires a physical infrastructure with relays on the water surface, which is largely ad-hoc, introduces a significant logistical overhead, and entails limited scalability. Our work, Sunflower, presents the *first* demonstration of wireless, 3D localization across the air-water interface – eliminating the need for additional infrastructure on the water surface. Specifically, we propose a laser-based sensing system to enable aerial drones to directly locate underwater robots. The Sunflower system consists of a queen and a worker component on a drone and each tracked underwater robot, respectively. To achieve robust sensing, key system elements include (1) a pinhole-based sensing mechanism to address the sensing skew at air-water boundary and determine the incident angle on the worker, (2) a novel optical-fiber sensing ring to sense weak retroreflected light, (3) a laser-optimized backscatter communication design that exploits laser polarization to maximize retroreflected energy, and (4) the necessary models and algorithms for underwater sensing. Real-world experiments demonstrate that our Sunflower system achieves average localization error of 9.7 cm with ranges up to 3.8 m and is robust against ambient light interference and wave conditions.

CCS CONCEPTS

• **Hardware → Sensor devices and platforms**; **Sensor applications and deployments**.

1 INTRODUCTION

Underwater robots/sensors play a critical role in advancing explorations and monitoring of the underwater world. High-impact applications include inspection of aging national infrastructure and prevention of water pollution [62, 97]. To enable such applications
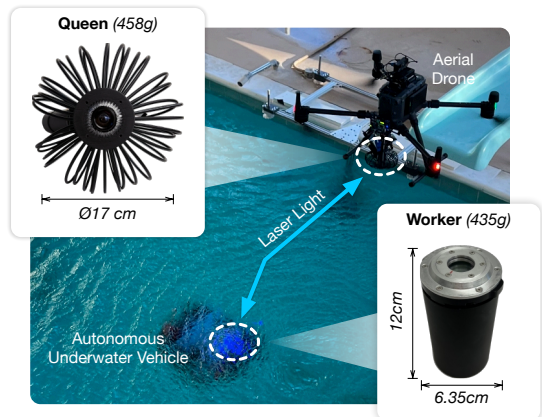
Figure 1: Sunflower in action. With a queen component on an aerial drone and a worker component on an underwater robot, Sunflower enables the drone to locate the underwater robot without surface relays.

and scale up the use of underwater assets, it is important to obtain their global locations during deployment. However, unlike land technology, there is no underwater global localization infrastructure. Instead, most existing technology focuses on dead reckoning through inertial or acoustic sensors [73].

For global sensing of underwater assets, the mainstream method relies on an infrastructure (e.g., a boat, a network of buoys) temporarily deployed on the water's surface [33, 57, 84]. The infrastructure is connected to both underwater assets (via acoustic transducers, completely in the water) and the ground station (via tethering or Wi-Fi). The logistical and deployment overhead of these surface buoys or vehicles constrains sensing coverage, resulting in limited scalability. Additionally, since floating surface buoys follow the current, they offer limited mobility for proactive control. Therefore, it is recognized in the robotics community that using flying vehicles with a bird's eye view to directly sense underwater assets will advance such efforts [80, 82]. Not only do flying vehicles expand the sensing coverage, but also offer greater control over mobility and deployability. To realize this goal, it is essential to allow aerial drones to directly sense underwater nodes without surface relays.

Current technologies for wireless localization mostly consider a single physical medium and are thus inapplicable in the air-water setting. For example, localization with radio frequency (RF) signals has shown the appealing capability of motion tracking in the air [50, 83, 90], however these same RF signals would suffer severe attenuation in the water [55, 87] and could not sustain reasonable localization distances. Additionally, although acoustic sensing is the mainstream method for locating underwater robots [33, 46, 57, 84], these acoustic signals cannot cross the air-water boundary and thus preclude direct air-water sensing. Another relevant technology is underwater imaging [39, 40, 43, 45, 81], where recent works [40, 45]

have studied remote imaging of underwater objects. However, these studies have not demonstrated the ability of 3D localization.

In this paper, we study the potential of direct air-water 3D localization using laser light, with the goal of enabling an aerial drone to locate underwater robots without any surface relays (Figure 1). Light is the most suitable medium because it can effectively pass the air-water interface with less than 10% energy reflected back (when the incident angle is <50° [36]). Compared to acoustics, light propagates faster and entails shorter communication/sensing latency. Compared to RF, light endures much lower attenuation in the water; light in the blue/green region (420 nm – 550 nm) attenuates less than 0.5 dB/m in water [10, 55]. We specifically consider blue/green laser light due to its superior sensing properties including (1) narrow (5-10nm) spectral power distribution, allowing optical energy to be concentrated to the wavelength range with the smallest attenuation in the air/water, and (2) low beam divergence, which maximizes the energy efficiency and enhances communication/sensing distance.

Our key contributions are within Sunflower, the *first* demonstration of 3D localization across the air-water boundary. Borrowing from the hierarchy of bees, Sunflower comprises a *queen* component on the aerial drone, and a *worker* component on each underwater robot to be located. To sense the worker from the air, the queen steers a narrow laser beam and senses the light reflected by the worker. We exploit the retroreflection phenomenon by attaching a retroreflective tag to the worker. A retroreflective tag reflects incoming light back to the source, easing the identification of the underwater robot's direction. Sensing based on retroreflected light also eliminates the need of any active emitter on the worker, leading to a simplified system design. Our main technical elements address numerous practical challenges in this scenario. *First*, we design a pinhole-based sensing mechanism for the worker to determine the incident angles of the laser beam, which resolves the challenge of the difference between the incident angle on the water's surface and on the underwater worker. *Second*, to sense extremely weak retroreflected light across the air-water boundary, we propose a novel optical fiber sensing ring on the queen to enlarge the sensing area and improve sensing sensitivity. We also build backscatter optics tailored to laser light, which exploits the polarization of laser light to maximize the energy of retroreflected light, and judiciously choose a backscatter modulation scheme to combat ambient light interference. *Third*, we develop an adaptive sensing algorithm that is robust to water dynamics.

We implement and fabricate a Sunflower prototype using off-the-shelf hardware and custom printed circuit boards (PCBs). We have extensively tested our prototype in a water tank and pool, and examined its performance of locating a mobile underwater robot from a flying drone. Our key findings are:

- Sunflower locates an underwater robot (1.75 m deep) from the air (1.6 m high) with an average error of 5.5 cm in a water tank and 9.9 cm in a pool. This performance supports mapping and data collection in shallow-water (<3 m) regions, inaccessible to vessels [58], with an error that is comparable or better than other visual-based estimation systems [52] and well within the few meters of the GPS uncertainty [42].
- Sunflower's sensing range is dictated by the success of laser-optimized backscatter communication, which achieves 90% packet

success rate up to a 3.8 m air-water distance (2.3 m air, 1.5 m water) with a 100-mW laser beam.
- The accuracy of Sunflower's angle-of-incidence sensing is stable across the worker's entire sensing range (-50° to 50°) with an average error of 1.2°.
- When evaluated on a mobile drone and moving underwater robot, Sunflower achieves an average localization error of 8.98 cm with a standard deviation of 2.03 cm, despite the presence of waves, ambient light, vibrations, and movement.
- Sunflower is robust against ambient light interference, waves, and disturbances affecting AUV station-keeping, a problem especially present in shallow waters.

A video [32] of the Sunflower system demonstration is available at:
https://youtu.be/ofpqm2G2s_U

2 AIR-WATER SENSING CHALLENGES

Achieving accurate air-water sensing using laser light presents a number of practical challenges.

Sensing Skew at the Boundary. The air-water context complicates the geometry for locating underwater robots from the air – specifically because of the refraction occurring at the air-water interface. To illustrate this challenge, consider a conventional laser-based localization system in a single medium [59, 64, 75]. First, a laser transmitter emits a beacon signal modulated with its position information and outgoing beam angle. Once the laser beam reaches the receiver, the transmitter's outgoing beam angle and position information can be extracted. This scheme, however, fails to work through the air-water interface since light refracts according to Snell's law [25, 51], causing the incident angle on the air-water boundary to differ from the incident angle on the underwater receiver. Consequently, the underwater robot would incorrectly localize itself relative to the transmitter if it only relied on the transmitter's information.

Furthermore, assuming the refractive indices were known ahead of time and the receiver used Snell's law to compute the underwater incident angle, this would only support static air-water interfaces. In the real world, however, air-water boundaries are dynamic and composed of ever-changing waves [30, 74]. Hence, for a given outgoing beam angle, the refracted angle through the water's surface will change depending on the position the light hits the wave at [36]. If the receiver ignores this inevitable scenario, the computed localization will oscillate depending on the wave shape, leading to consistently incorrect localization results [36].

Sensing Extremely-Weak Retroreflected Light. The air-water scenario also weakens the retroreflected light traveling across the air-water boundary *twice*. Robust sensing of this extremely-weak retroreflected light is critical to maintaining a meter-level sensing range sufficient for robotics applications. As the laser light travels through the air, it undergoes free space path loss inversely proportional to its wavelength [54, 72]. Once the light hits the air-water interface, up to 10% of the light is reflected (as long as the incident angle is below 50°) [25]. Then, as the light travels underwater, it undergoes attenuation proportional to its wavelength (in the visible light region) [55]. Finally, once the light hits the underwater retroreflector, the retroreflective loss can be over 90% depending on the
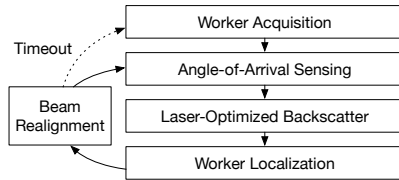
Figure 2: System flow of Sunflower.

incident angle and retroreflective material. After reflecting back to the aerial transmitter, the light beam will encounter the above loss once again: underwater attenuation, up to 10% loss at the boundary, and aerial attenuation. After summing all these potential losses, the received signal strength can easily be buried by noise. Since gain is often inversely proportional to response time, traditional photodiodes (e.g., [21]) would be unable to capture this faint amount of light. Furthermore, assuming an average level of ambient light at sea level, the received SNR could be as low as -14 dB [36] (assuming a 100 mW, 520 nm, off-the-shelf laser diode) – far too low to be received without additional filtering mechanisms. Additionally, these calculations all assume the backscatter receiver's photodiode is perfectly collocated with the outgoing laser beam. In reality, however, physical constraints require the receiver's photodiode to be placed with an offset relative to the outgoing beam.

Although the choice of retroreflective material can help reduce the energy loss during retroreflection, the most energy efficient options (e.g., corner-cube retroreflectors [27]) are large and rigid, making them impractical for sensing applications. Flexible retroreflectors (e.g., retroreflective tape [93]), on the other hand, can be seamlessly molded around various surfaces yet result in a large amount of specular and diffusive reflections. From our experiments, retroreflective tape reflects less than 40% of light compared to corner-cube retroreflectors. This is extremely unfavorable when coupled with the attenuation caused by the air-water boundary.

Ambient Light Interference. Compounding the above issues is the presence of ambient light interference. If a simple pulse detection strategy is used (i.e., triggering on the rising edge of a sensed pulse), it is easily prone to false positives caused by the environment. This is especially pertinent if the gain of the receiver is tuned high enough to detect the faint amount of retroreflected light. From our experiments, implementing an analog rising-edge pulse detector that was sufficiently sensitive to receive the backscattered light would falsely trigger multiple times per minute in the single-medium scenario. When coupled with water, where stray reflections are unavoidable, the false trigger rate was multiple times per second. Additionally, encoding the laser light with a unique frequency would be unsuitable for separating stray reflections from backscattered signals. This is because if the encoded laser light hits a reflective surface (e.g., water wave causing specular reflection back to the transmitter), the receiver would still detect the frequency signature despite not hitting the retroreflective target.

3 SUNFLOWER DESIGN

We present Sunflower to address the above challenges. To overcome the sensing skew at the boundary, instead of sensing the refraction angle, Sunflower relies on an angle-of-arrival (AoA) sensing component on the underwater robot which senses the incident angle after refraction from the current wave surface. To sense the

---

Algorithm 1: Adaptive Scanning.

1 **Initialization:** scan flag = 1, connected = 0, time out = 0
2 **while** *True* **do**
3   **if** *scan flag == true* **then**
4   scan flag = false
5   **if** *connected == true /*connection established*/* **then**
6   **if** *time out < threshold$_2$* **then**
7   current state = realignment
8   time out++
9   **else**
10   current state = acquisition
11   **else**
12   current state = acquisition /**never detected*/*
13   **if** *unique frequency detected && magnitude > threshold$_1$* **then**
14   connected = true /**found the robot*/*
15   decode backscattered data
16   **else**
17   scan flag = true /**robot not found, keep scanning*/*
18   connected = false

---

weak retroreflected light, Sunflower utilizes a novel optical fiber sensing ring to enhance the sensing sensitivity while easing the collocation of the photodiode and transmitter. To combat ambient light interference, Sunflower exploits the spectrum sparsity of laser light to filter out most ambient light energy.

Specifically, Sunflower consists of a *queen* and a *worker*. The queen resides on an aerial drone, and the worker is collocated with the underwater robot. The queen is composed of a laser steering and sensing component, while the worker contains the AoA sensing component and a retroreflective tag. Figure 2 illustrates the steps for the queen to locate an underwater robot. During link acquisition, the queen actively steers a laser beam to sense the light retroreflected by the worker, thereby identifying the robot directions. Once the queen's laser beam hits the worker, the worker senses its incident angle after the impact of refraction. It then sends its AoA and depth (sensed by robot's built-in depth sensor) back to the queen via backscatter communication. Finally, the queen combines this information with its own GPS location and altitude sensor, computing the worker's location in real time. We will next discuss each step in detail.

3.1 Robust Link Acquisition

The first step in air-water sensing is for the queen to find the presence of the worker and establish a communication channel. By exploiting the path symmetry of light, a single transceiver can steer its laser beam until it hits the other node's retroreflector, therefore instantly detecting when the link has been established. To realize this method, a key challenge is robust detection of retroreflected light from the worker/tag. Furthermore, although this method is faster than an active approach (i.e., having two transceivers coordinate with each other), scanning a sufficiently large range for the other node can take hundreds of milliseconds [36]. If either the aerial or underwater nodes move or the water changes the angle of refraction, the scanning phase will need to be repeated. Efficient free-space optics (FSO) algorithms cannot be directly applied, because despite their ability to scan a large area in an efficient amount of time, they do not consider frequent channel disconnections (e.g., every second) from node mobility/channel perturbations. To solve these challenges, we propose a novel optical design to sense ultra-weak retroreflected light and design a custom adaptive scanning
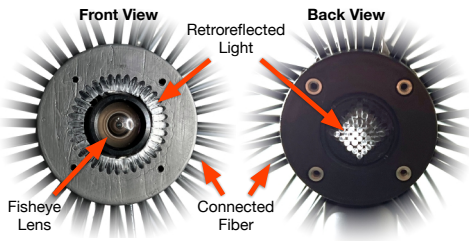
Figure 3: Fiber ring with light coming through.

algorithm (Algorithm 1) that (1) minimizes the tracking delay by separating initial acquisition from beam realignment, (2) exploits cross-medium refraction to increase scan coverage. We discuss additional improvements in §6 and elaborate on each major design element in the following paragraphs.

Sensing with Optical Fiber Ring To handle weak retroreflected light, we propose a novel optical design built upon an optical fiber sensing ring. As shown in Figure 3, the sensing ring is composed of optical fiber bundles that are evenly placed around the transmitter's fisheye lens. Given the flexibility associated with optical fiber (e.g., minimum bend radius of 25 mm [22]), the optical fiber can be collocated as close as possible to the transmitter's exit point, thereby maximizing the amount of backscattered light capable of being sensed. After the retroreflected light bounces back to the transmitter, it will illuminate the various optical fibers surrounding the transmitter's exit lens. The opposite end of the optical fibers are then diverted away from the transmitter's lens and combined to a single point, allowing the faint amount of retroreflected light to be aggregated to a single point. As a result, small, fast photodiodes (e.g., silicon photomultiplier sensors [49]) can be coupled with small-core fiber for high gain and high-sensitivity sensing. The use of the fiber bundles expands the sensing area, resulting into aggregated light with higher energy density being projected to the small sensing area of a high-gain photodiode. This design helps to sustain sensing at meter-level distances.

The fiber ring design also addresses the challenges of collocating photodiodes with light source. When the retroreflected laser light arrives back at the transmitter, it will have travelled along nearly the same path as it took to arrive underwater. Consequently, a photodiode should ideally be placed directly over the transmitting lens so that it can detect the majority of retroreflected light. This placement is impractical, however, as it would physically block the outgoing laser beam. Furthermore, placing the photodiode to the side would limit the amount of retroreflected light that could be received and also result in receiver blind spots. Although these blind spots could be reduced with larger photodiodes strategically placed around the exit point, the increase in size would come at the expense of photodiode's sensitivity.

Adaptive Scanning. To minimize the scanning delay, we propose splitting our scanning into two phases: acquisition and realignment. During the acquisition phase, we first calibrate once to get the environmental noise level for setting $threshold_1$ and then scan in an Archimedian spiral [4] pattern which is commonly used in FSO [78]. This pattern is useful for the acquisition stage as it can scan a large area in an efficient amount of time. After modifying the
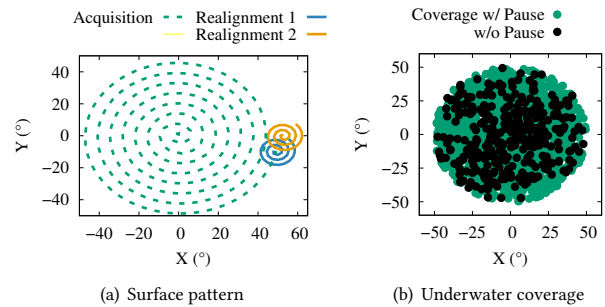

(a) Surface pattern

(b) Underwater coverage

Figure 4: Scanning pattern and coverage of link acquisition.

original spiral algorithm's step size to match our laser beam size, all points in the steering FOV are guaranteed to be hit. Once the link has been acquired, we then switch to our realignment scan pattern, i.e., a modified version of our acquisition pattern that targets a smaller area immediately close to the last known position. This allows the system to quickly find the next surrounding position of the underwater node while also ensuring that the next position is not missed. Only when the underwater robot cannot be found after a certain amount of time (i.e., Algorithm 1 line 8: $threshold_2$ is set as the time duration for two full cycles of the realignment scan), the acquisition scan will be triggered again. Figure 4(a) shows a complete scan pattern with two realignments in calm-water.

Exploiting Wave Dynamics. Furthermore, we leverage the movement of water waves to increase our scanning coverage by delaying each scan point (i.e., pausing the scan for a certain amount of time at a fixed steering angle), thereby allowing the refracted beam to hit multiple underwater positions for a single outgoing angle. Since the queen identifies a worker by its unique tag frequencies, it must receive a certain amount of data before applying the Fast Fourier Transform (FFT). For example, if the lowest tag frequency is 500 Hz, the queen requires at least 2 ms worth of data for the FFT. To validate this scanning methodology, we simulate the water's surface with a sinusoidal wave model that is widely used for synthesizing water waves [44, 77]. Figure 4(a) demonstrates the acquisition scan pattern underwater without the presence of waves. As shown in Figure 4(b), after adding the water waves in, the coverage area decreases to 77.2% without pausing at each point. However, with a 2 ms pause, the coverage area remains above 91%.

3.2 Angle-of-Arrival Sensing

Once the laser beam hits the worker, the next step is for the worker to derive beam's incident angle. Given the inevitable presence of water dynamics – which makes it difficult to simply compute the refracted angle via Snell's law – our design proposes a pinhole angle-of-arrival (AoA) sensing mechanism that allows real-time, medium-independent localization. Existing AoA sensing techniques typically require an array of photodiodes [34, 60], which is not suitable in our case since a large beam size is required to guarantee each PD is triggered. However, a large beam size would severely decrease our sensing SNR. Although commercially available laser AoA sensors are available [11], they are very expensive (≥$5000) and also less sensitive to blue wavelengths. We instead propose combining a pinhole iris with an image sensor to create a low-cost, fully integrated AoA sensing mechanism for laser light applications.
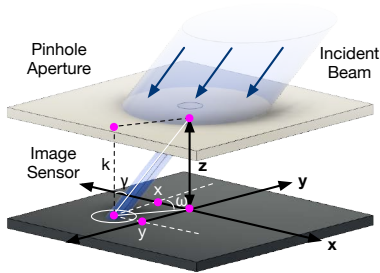
Figure 5: AoA sensing rationale.

As shown in Figure 5, with a small (e.g., 500 μm) pinhole mask above an image sensor with distance k, the laser beam produces a tiny spot, whose position is dependent on the incident angles γ and ω. Here γ is the incident angle with respect to the vertical norm (i.e., the z axis) of the image plane, while ω is the angle with respect to the y axis. Combining the location of the spot on the image sensor, (x, y), with height k, we can derive γ and ω as:

$$\gamma = \arctan\left(\frac{k}{\sqrt{x^2 + y^2}}\right), \ \omega = \arctan\left(\frac{y}{x}\right). \tag{1}$$

Our application only requires γ to locate the underwater robot since ω only determines the robot's yaw angle, which in practice can be determined with an inertial measurement unit (IMU) installed on the robot. Additionally, the rotation angle ω can be useful for other applications (e.g., underwater robot attitude control and commanding specific directions [79, 85]).

Spot Location Detection. Since both ambient light and laser light will pass through the pinhole mask, a constant light spot will appear on the image sensor regardless of the presence of laser light. Adding an optical bandpass filter can remove the influence of ambient light from the AoA sensor. However, optical bandpass filters are often limited to $\le 5°$ incident angles (thereby limiting our sensing range). Instead, we leverage the fact that our laser light has a much higher energy density than the sunlight, and reduce our image sensor's exposure time accordingly. Specifically, by reducing the exposure from several milliseconds (which causes both spot sizes to appear equal in size as the image sensor is saturated at these intensity levels) to several microseconds, the spot size corresponding to the laser light will be larger than the one corresponding to the ambient light. Therefore, we can set a threshold to filter out the smaller of the two spots. Once we obtain the laser light spot, the next step is to derive its location on the image sensor. Since the beam size is much larger than the pinhole, the spot shape is the same as the the pinhole (i.e., a circle). Thus we use the center of the spot to represent its location. We compute the actual center of the spot, (x, y), by taking the average over the pixel coordinates whose intensity values are higher than the given threshold. After getting the distance (k) between the pinhole mask and the image sensor during calibration, we can derive the incident angles with Equation (1), regardless of the refractive index mismatch between the two mediums.

3.3 Laser-Optimized Backscatter

After AoA sensing, the worker reuses the laser beam to send back the AoA results and its depth value (acquired by the robot's built-in depth sensor) via a backscatter communication channel. The use of backscatter minimizes sensing delay and better supports constant water dynamics and link mobility. Existing light-based backscatter systems generally consider LEDs as light emitters and all rely on LCD shutters to modulate the backscattered light [91, 92, 98]. Fundamentally, an LCD shutter consists of two orthogonal linear polarizer, one placed on each surface of a liquid crystal polymer. By applying a voltage to the liquid crystal, the twist state of the liquid crystal changes, either allowing the polarized light to pass through or be blocked. This design, however, entails significant energy loss when coupling with LEDs. Specifically, since light emitted from LEDs is inherently unpolarized, when it passes through the first linear polarizer, half of the energy is blocked and therefore wasted.

We propose to exploit the polarized nature of laser light to circumvent such energy loss and boost the energy efficiency of light-based backscatter communication. Specifically, since laser light is inherently linearly polarized, we can remove the first linear polarizer on the LCD shutter, thus increasing the efficiency from the conventional 50% up to 100% (essentially limited by the polarization percentage of the laser diode). However, since the linear polarization direction of the laser light changes as the emitter rotates, the incident light on the LCD shutter might be completely perpendicular to the second polarizer. Consequently, adopting a conventional light-based backscatter design directly with LDs would result in the amount of backscattered light to range from 0% to 100%, leading to instability and high error rates of demodulation.

To maximize the retroreflected light energy regardless of the laser or shutter's orientation, we propose a novel system design that converts linearly polarized laser light to circularly polarized laser light boosting the robustness against laser/shutter rotation. This conversion is achieved via a pair of quarter waveplates. As shown in Figure 6, we align the first quarter waveplate with the laser diode such that the polarization direction of the laser light is 45° relative to the fast axes of the quarter waveplate. With this alignment, the linearly-polarized laser light becomes circularly-polarized, meaning the magnitude of polarization is constant along the axis of propagation. Similarly, on the underwater node, we align the second quarter waveplate's fast axis 45° relative to the polarization direction of the LC shutter in its open state. This transforms the circularly polarized laser light back to linearly polarized light and ensures that the polarization direction is parallel to the LC shutter when open. Then, by changing the voltage of the LC shutter, we can pass or block up to 100% of the incident laser light from hitting the retroreflector. The relative rotation between the first and the second quarter waveplate will not change the linear polarization direction before or after the transformation. Thus, once the polarization alignment on both nodes is fixed, the polarization direction of the laser light will be perfectly parallel to the backscatter node's LC shutter when open, and perfectly perpendicular when closed – regardless of the relative movement between the aerial and underwater nodes.

A prior work [63] applied a similar concept to boost the communication performance of LEDs underwater. Their use of circularly-polarized light was to create two parallel communication channels while dealing with receiver orientation changes. Our design differs in applying the concept to the context of backscatter communication, and most importantly, leveraging the unique properties of laser light to to increase the backscatter efficiency of a single channel by up to 50%. Consequently, we can remove the lossy linear polarizer on the queen and bandpass filter on the worker.
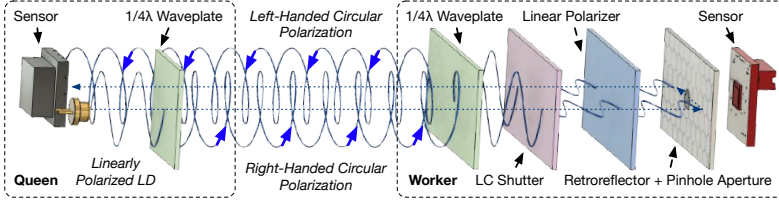
Figure 6: Laser-optimized backscatter optics.

Figure 7: Geometric model of localization.

Backscatter Modulation. Additionally, we apply frequency-shift-keying (FSK) modulation for our backscatter communication. FSK is more robust than other modulation schemes such as On-Off Keying (OOK), which relies on the single rise of light intensity to encode data and can be falsely triggered by ambient light variations or reflection from other surfaces. With FSK, we choose high frequencies (e.g., above 500 Hz) that are not common in the environment to avoid the false triggering from ambient light. To deal with the rare cases where ambient noise sources have frequencies close to the frequencies chosen for our FSK implementation, we add an initial calibration step that collects one-second of ambient light data (with the laser off) and computes the maximum energy magnitude at our frequencies of interest. This magnitude is then set as the threshold for detecting the backscatter tag. We also add a voting-based frequency determination procedure coupled with a sliding window in our decoding scheme. Specifically, we first synchronize the received data by correlation analysis of the preamble. Then we leverage a sliding window to loop through the synchronized data and take the mode of all the dominant frequency elements of each trial as the final dominant frequency for each bit. In this way, the decoding is more robust to imperfect synchronization caused by noise. An additional benefit of FSK is the differentiation of multiple robots, which we discuss in §6.

3.4 Computing Robot Location

After receiving the depth and AoA information from the backscatter channel, the queen can combine them with the laser's steering angle and its altitude to compute the precise location of the underwater workers. As shown in Figure 7, an aerial drone (A) is h meters above the water's surface, communicating with an underwater robot (B), which is d meters below the water's surface. In order to locate the underwater robot, we need to know the distance between $A'B'$ ($d_{A'B'}$) and the azimuth angle ϕ. A' and B' are the vertical projections of A and B onto the flat water surface and O' is the incident point. If we set A' as the origin of the coordinate system, the coordinate of the underwater robot relative to the aerial drone can then be derived from:

$$(X, Y) = d_{A'B'} * (\cos \phi, \sin \phi). \tag{2}$$

$d_{A'B'}$ can be further divided into $d_{A'O}$ and $d_{OB'}$. $d_{A'O}$ can be computed from the height of the drone (h), and the elevation angle (θ) of the laser scanning, where h, θ (together with ϕ) are provided by the drone's altitude sensor and the laser beam steering controller. To compute the second distance ($d_{OB'}$), we require the depth of the underwater robot (d) and the angle between the vertical line and the refraction line (γ). If the water was a flat surface, the incident angle from the air to the water (α) would be the same as the elevation
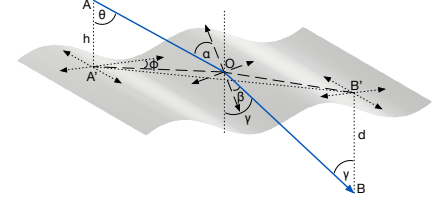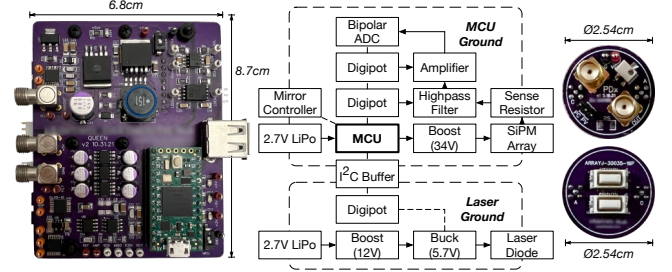

Figure 8: Block diagram of the queen's circuit.

angle (θ), and the refraction angle (β) would be the same as γ. Then, using Snell's law, we could derive γ. However, as stated above, $\gamma \neq \beta$ due to wave dynamics. One potential solution is to sense and model the water's surface in real time and find out the normal plane of the incident point. Unfortunately, this is computationally expensive and physically difficult to deploy [36]. Additionally, although the refractive index of the water (which is necessary for deriving γ) can be measured with a refractometer [24], they typically cannot be interfaced with a microcontroller (MCU). Thus, instead of using Snell's law, we propose to sense the angle of arrival (γ) with our pinhole design on the receiver side. The coordinates of the underwater robot then become:

$$(X, Y) = [h \tan \theta + d \tan \gamma] * (\cos \phi, \sin \phi). \tag{3}$$

It is worth noting that this geometry relationship is only satisfied with the assumption that A' and B' are on the same plane, which means the measurement of h and d should be relative to a flat water surface. We will present the localization error analysis on the influence of the wave in §5.

4 PROTOTYPE IMPLEMENTATION

Queen. We highlight following component of the queen implementation. *(1) Laser Driver.* The queen's laser is configured as a continuous wave (CW) to reduce system complexity. As shown in Figure 8, our queen utilizes a simple constant-voltage driver circuit capable of supplying up to 1 A of current to the laser diode. The laser power is supplied by a 10050 mAh 3.7 V LIPO battery, boosted to 10 V using a switching voltage regulator [14], then linearly regulated down to the laser's operating voltage using an LM317. The laser voltage is electronically controlled by an I^{2}C digital potentiometer [16], allowing mV-resolution adjustments from a single MCU (Teensy 4.0). To reduce noise, the laser driver resides on a separate ground plane than the other digital components, and communicates with the MCU using GPIO and I^{2}C isolation buffers [2, 3].

(2) Beam-Steering Circuit. We achieve wide-angle beam steering with a custom optical circuit design (Figure 9 (right)). Aside from
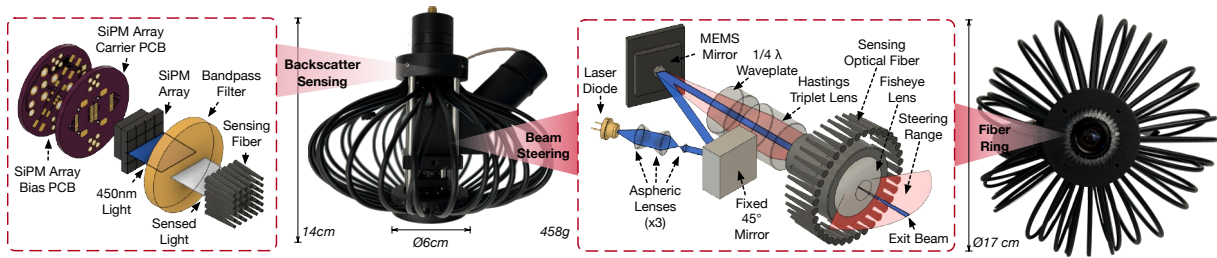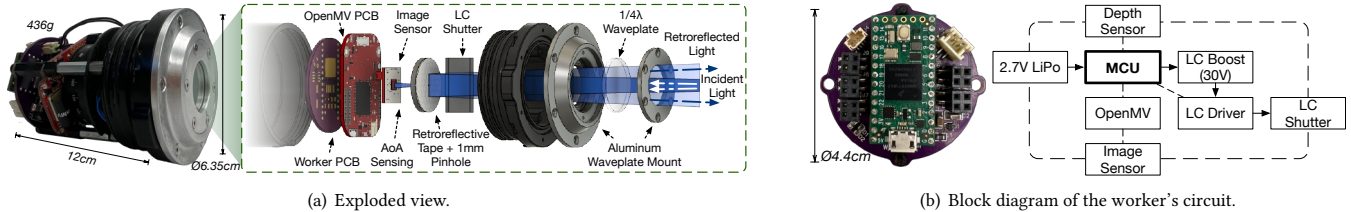
Figure 9: Overview of the queen, with exploded view of backscatter sensing and beam steering.

(a) Exploded view.

(b) Block diagram of the worker's circuit.

Figure 10: Worker implementation.

the MEMS mirror, other optical components are all passive. The queen's laser diode (450 nm, nominally 80 mW, Osram PLT5450B) is collimated using a single aspheric lens [7] with a focal length (2.76 mm) large enough to place the lens at laser diode's focal point. The beam is then converged to a single point with an equivalent aspheric lens [7] and oriented 180°. A short focal length aspheric lens [6] is placed at this focal point, allowing the originally large collimated beam diameter (5 mm) to be reduced to a smaller beam diameter (2 mm) suitable for the remaining optical elements.

The collimated beam is then coupled to a 3D printed mount, reflecting the beam off of a fixed-angle mirror [23] and onto our MEMS mirror [18] with an angle-of-incidence (AoI) of 22°. The MEMS mirror is connected to a Mirrorcle USB-SL MZ controller which is controlled by our MCU using a USB serial interface. After reflecting off the MEMS mirror, the steered beam passes through an infinite conjugate ratio triplet lens [28] to focus the outgoing beam and correct the AoI for the remaining optical elements [36]. Then a quarter waveplate [9] is positioned in a rotation mount just after the triplet lens. The quarter waveplate is aligned 45° relative to the laser's measured polarization direction (98% polarized) and converts the light to circularly polarized (confirmed with a polarimeter[26]). Finally, the circularly polarized light passes through a fisheye lens [8] for an expanded steering range. The position between the triplet lens and fisheye lens dictates the divergence of the outgoing beam and is experimentally fixed to 1° (half 3dB-divergence angle) to provide optimal beam quality. After passing all optical components on the queen, the 133 mW laser diode (overclocked from the nominal 80 mW value) was measured to be 100 mW, indicating a 24.8% loss.

(3) Backscatter Receiver. Figure 9 (left) shows the exploded view of the optical fiber ring. The diverted light passes through an optical bandpass filter [12] tuned to the wavelength of the queen's laser. After passing the filter, the monochromatic light is free-space-coupled to an extremely high gain 4×4 silicon photomultiplier (SiPM) array [5] matched to the size of the exit fiber bundle. A custom PCB treats all SiPM array elements as parallel current sources, biased to 32 V using a switching voltage regulator [15] on a separate PCB. The current is then converted to a voltage with a variable resistor, and fed over an SMA cable to the backscatter receiver.

We design and fabricate a custom PCB for the backscatter receiver (Figure 8). It first AC-couples the SiPM voltage with a fixed capacitor and digital potentiometer [16], allowing the waveform to be electronically tuned by the MCU. The filtered signal then passes through an impedance matching buffer [19] which also amplifies the signal using another digital potentiometer (allowing electronically adjusted gain). Since the signal is now AC-coupled, the bipolar signal is sent through a bipolar ADC [1] which connects to our MCU over SPI. We implement FSK demodulation and localization logic using C/C++. We set the ADC sampling rate to 16 kHz with a symbol duration of 2 ms, resulting in an FFT frequency resolution of 500 Hz. As mentioned in § 3.3, we implement a sliding window decoding strategy with window size 32 and step size of 1. In our experiments, we utilize Reed-Solomon coding [76] to correct up to 3 incorrect bits, reserving 24 bits for data and 6 bits for parity.

Worker. The worker implementation contains following modules. *(1) Worker Optical Circuit.* Figure 10(a) shows the connection of all hardware components on the worker. To minimize the effects of refraction, the quarter waveplate directly contacts water, sealed between two O-rings and air-tight coupled to the underwater enclosure with a custom milled aluminum cap. Directly below the quarter waveplate is a liquid crystal PiCell shutter [31], capable of changing its linear polarization state up to a few kilohertz. Since the incident light is now linearly polarized 45°relative to the fast-axis of the quarter waveplate, the shutter is oriented so its linear polarization is 45°relative to the quarter waveplate's fast axis. The shutter is controlled electronically by the worker's MCU for backscatter modulation. The FSK modulation logic runs on the Teensy 4.0 with an implementation in C/C++. We set the synchronization/two data frequencies to 500 Hz, 1k Hz and 2k Hz, respectively.

The AoA sensing apparatus is then placed directly below the retroreflector. Specifically, we place retroreflective tape atop a 500 μm diameter pinhole (Thorlabs P500K). An OpenMV image sensor[20] lies directly below the pinhole's aperture, connected via a ribbon cable to the main OpenMV controller. We leverage the MicroPython libraries [17] for blob detection and send the pixel coordinates of the laser spot to the worker's MCU over a serial connection.
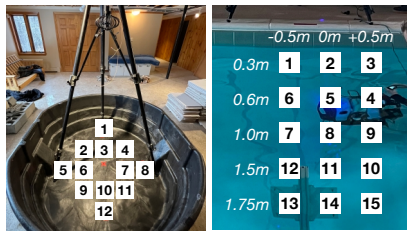
(a) Water tank.   (b) Pool.

Figure 11: Experimental setup.

(a) Error across locations.   (b) CDF.

Figure 12: Experiment results in the water tank.

The AoA result takes approximately 50 ms to compute and is processed simultaneously with the backscatter communication (i.e., the backscatter data contains the last fully completely AoA result).

(2) Worker Controller and Waterproof Enclosure. Figure 10(b) shows the circuitry of the worker PCB. To drive the PiCell shutter, a Microchip HV508 driver is coupled with a simple switching voltage boost regulator [14] to achieve the correct drive voltage and pulse frequency (i.e., 100 kHz square wave alternating between 3.3 V and 30 V depending on the shutter's state). The OpenMV is connected via SPI to the worker's MCU, and its PCB is shaved down to fit within a waterproof enclosure (aluminum tube with 2-inch diameter), which contains a custom USB cable and a Bar02 pressure sensor to provide depth measurements for the localization algorithm. A custom USB PCB is soldered to provide remote USB, GPIO, and reset access to the internal controller during experiments.

5 EVALUATION

We now evaluate the localization accuracy, range, and robustness of Sunflower in a variety of scenarios.

5.1 Localization Accuracy

We examine the accuracy of our localization methodology in two setups (Figure 11): (1) a large water tank (1.6 m × 1.75 m × 0.63 m) filled with chlorine water and (2) an indoor swimming pool (7 m ×25 m ×1 m to 3 m). The illuminance was approximately 500 lx throughout our water tank experiments, and 1500 lx throughout our pool experiments. Since all experiments were performed indoors – precluding the use of GPS – the queen remains fixed in the air rather than attached to a mobile drone. We compare two baselines to our Sunflower accuracy: the single-medium sensing case (i.e., without the presence of water) and the cross-medium sensing case (i.e., with water but not using the worker's sensed AoA).

Calm Water Surface. We start by considering a controlled water environment where we can manually provide the ground truth with known accuracy. To provide the most accurate ground truth, we manually mark twelve locations uniformly spread on the bottom of a large water tank (Figure 11(a)). Each location is 25.4 cm apart from adjacent locations. The queen is fixed to a tripod 1.65 m in the air (maximum height to the ceiling) and placed at the center of the tank, looking downwards. For each of the twelve locations, the worker is placed so the plane of its quarter waveplate is parallel with the plane of the queen.

To first confirm the single-medium accuracy, we place the worker at each marked location before filling the tank with water. As shown
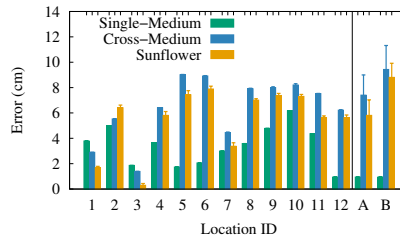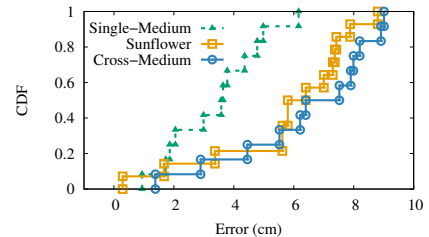
in Figure 12(a), we plot the localization error for each ground truth location, defining the error as the Euclidean distance between our derived worker locations and the ground truth locations. For each location, 100 position samples are collected by the queen and averaged, with error bars showing the standard deviation per point. Across all points, the average single-medium localization accuracy of our system is 3.4 cm with a standard deviation of 1.5 cm.

We next add water to evaluate the cross-medium accuracy and Sunflower accuracy. First, we fill the water tank with 30 cm of water, effectively placing the worker 15 cm from the air-water interface and at 1.5 m distance to the queen. Second, we repeat the above error calculations for each point in the presence of calm water. Notably, across all points, the average cross-medium localization offset of our system is 6.4 cm with a standard deviation of 2.5 cm. Adding in our Sunflower design, we achieve an average localization error of 5.5 cm with a standard deviation of 2.4 cm – corresponding to 3.6% (error) and 1.6% (standard deviation) of the total distance between the queen and the worker (1.5 m). Figure 12(b) compares the distribution of location errors. The difference between the cross-medium baseline and our Sunflower system performance is small in this experiment as the depth of the water is only 15 cm, limiting the influence of refraction.

Increasing the Depth. Having established the low-error and high-stability of our system, we next investigate the impact of deeper water depths that were impossible to achieve in the water tank. The queen is fixed to a tripod 1.65 m in the air and placed at the edge of the pool (Figure 11(b)). Since manual ground truth measurements are prone to human-error in a large-scale pool setting, and using an aerial drone indoors precludes the use of GPS, we instead used a fiducial marker in a known position to localize an underwater robot with the worker. Fiducial markers are commonly used as ground truth measurements of relative positions at close ranges in underwater environments [61, 89]. Specifically, our robot utilizes a proportional-integral-derivative (PID) controller to maintain a stable position by sampling the fiducial marker with its monocular camera and making small corrections, with a maximum offset of approximately 10 cm from the target location in a single trial.[1] As a result of the robot's position corrections and water flow through the pool drain, approximately 2 cm waves are present on the surface of the pool. Additionally, the ambient light in the pool area was approximately 10,000 lx. We attach the worker to the robot and steer the robot to fifteen predefined locations as shown

---

[1]Location measurements provided by fiducial markers underwater have been shown to be Gaussian distributed with mean near ground truth [61].
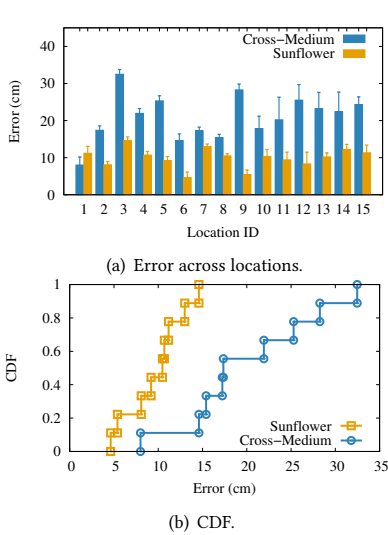
(a) Error across locations.

(b) CDF.

Figure 13: Experiment results in the pool.

(a) Distance.

(b) Angle.

Figure 14: Range test for backscatter communication and AoA sensing.

(a) Waves.

(b) Light.

Figure 15: Impact of wave conditions and ambient light.

in Figure 11(b) with depths of 0.3 m, 0.6 m, 1.0 m, 1.5 m, and 1.75 m (deepest achievable with a 100-mW laser beam).

As shown in Figure 13(a), the average localization error across all fifteen positions without our AoA sensing component is 20.9 cm, with a standard deviation of 6.1 cm. After adding the AoA sensing in, our Sunflower system achieves a localization error of 9.9 cm with a standard deviation of 2.6 cm – corresponding to 2.9% (error) and 0.7% (standard deviation) of the total distance between the queen and the worker (3.4 m). Figure 13(b) further illustrates the significant improvement of Sunflower over the baseline without AoA sensing. This performance of the Sunflower system is consistent with the tank experiments, and validates that our AoA sensing component is essential when dealing with deeper water depths.

Furthermore, due to environmental noise and the current caused by the pool drain that physically moved the underwater robot, the robot was constantly adjusting its position at each of the nine target locations. Despite this effect, the queen was able to maintain contact with the worker 90% of the time (on average) after the initial acquisition, benefiting from the beam realignment scheme outlined in §3.1. This validates that our Sunflower system is robust to disturbances affecting the station-keeping of underwater robots, which is especially present in shallow waters [88].

Comparison to Other Systems. The reported accuracy of a commercially-available "underwater GPS", based on a short baseline acoustic (SBL) positioning system – composed of 4 transducers at the surface and one on the underwater robot – is 1% of distance between the transceiver and the object [29]. Although this ideal value is comparable with our system accuracy, we were unable to identify any real-world experiments that validate its legitimacy. In practice, many factors affect the real-world accuracy of any acoustic positioning system, including errors in the geometric configuration of the transducers and of the utilized sound profile [62]. The closest experiments found in prior work use an ultra short baseline (USBL) system which has frequent location jumps within a few meters [86]. In comparison, Sunflower system provides significantly greater
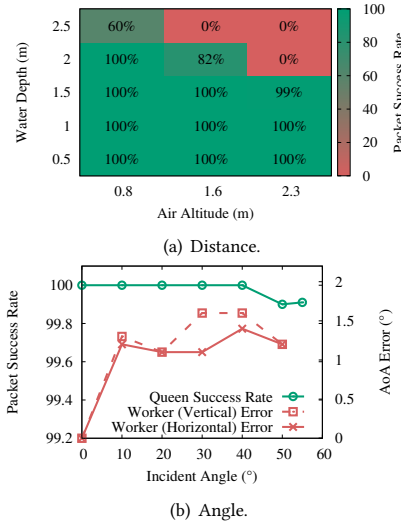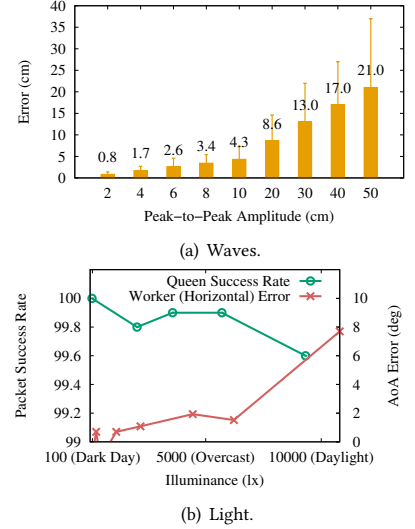
localization accuracy without meter-level jumps. Additionally, it is worth stressing that none of the above-mentioned systems are capable of cross-medium sensing, as acoustic signals cannot pass through the air-water boundary.

Dynamic Water Surface. We now investigate the accuracy of our system in the presence of waves. To ensure that our ground truth measurement is accurate, we place the worker at location twelve (Figure 11(a)) which has the lowest single-medium error (and therefore highest ground-truth accuracy). Furthermore, location twelve was chosen to be farthest from the center of the tank, thereby ensuring a longer transmission distance and non-zero incident/retroreflected angle. Two wave conditions are manually generated by a rigid panel: wave A having an approximate peak-to-peak amplitude of 10 cm and wave B having an approximate peak-to-peak amplitude of 20 cm. As shown in Figure 12(a), wave A caused an average localization error of 5.8 cm ± 1.23 cm and wave B caused an average localization error of 8.8 cm ± 1.12 cm. Given the range of waves typically found in nature (e.g., 2 cm to 20 cm [36]), our system is still applicable with this level of wave dynamics. We explore a variety of other wave conditions using a theoretical analysis in §5.4.

5.2 Supporting Range

Having demonstrated the localization accuracy of our system, we next explore the maximum sensing range that we can support. Since our sensing inherently relies on the correct reception of backscattered packets, we define our maximum range according to the packet-level correctness of the communication channel. In other words, if a packet containing crucial localization information can be correctly decoded, then sensing at this range is achievable. Consequently, our sensing range can be written in terms of the *packet success rate*, i.e., $(1 - \text{PER}) \times 100$ where PER is the packet error rate after RS coding. In the same pool environment, we attach our worker to an underwater tripod and our queen to a tripod on the edge of the pool. For each position of the worker, we raise/lower
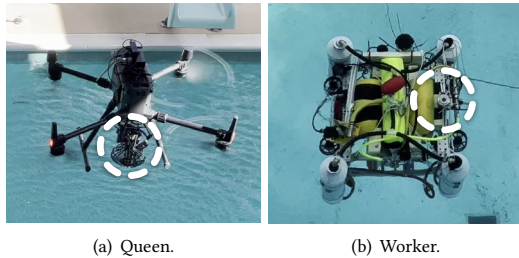
(a) Queen.   (b) Worker.

Figure 16: Mounting Sunflower on a drone and underwater robot.

Figure 17: Accuracy of locating an underwater robot from a drone.

the tripod to three different distances spanning 0.8 m to 2.3 m. By slowly moving the worker along the bottom of the pool, we increase the depth from 0.5 m to 2.5 m. As shown in Figure 14(a), we achieve a packet success rate of 100% in most transmission scenarios – including an over 99% packet success rate up to a 3.8 m air-water distance (2.3 m air, 1.5 m water) – which is sufficient for many underwater robot applications [35, 71]. Finally, it is worth noting that the current range results are achieved with a low-power (100 mW) laser beam with a 1° half 3-dB beam divergence. Additionally, the total laser propagation distance is twice the physical queen/worker distance due to the backscatter communication channel. In §6, we discuss extending the range for additional maritime applications.

Additionally we evaluate the angular sensing range of the queen and worker. To measure the angular range of the worker, we rotate the worker both vertically and horizontally so that the incident angle changes until the center of the beam spot reaches the two edges of the image sensor. As shown in Figure 14(b), our worker can support AoA sensing between -50° and 50° on both axes. Furthermore, the AoA sensing error is stable across the whole sensing range with an average error of only 1.2°. To measure the angular range of the queen, we rotate the worker to various fixed angles and have it transmit a fixed payload. We then quantify our angular sensing range according to our packet success rate. As shown in Figure 14(b), our packet success rate is over 99% for the entire optical steering range (i.e., -55° to 55°).

5.3 Locating Mobile Robots from Flying Drones

We now evaluate the complete setup with an aerial drone and underwater robot. As shown in Figure 16, we fix the queen onto the front of the aerial drone and the worker to the side of the underwater robot. First, we program the underwater robot to position itself at six evenly-spaced locations in a $1\ m \times 1\ m$ grid positioned 0.3 m below the surface.[2] Second, the queen is programmed to fly 1.5 m above the grid, periodically changing its x-y position to emulate real-world drone mobility. Third, the queen scans its laser beam in a spiral until it hits the underwater robot, where it collects localization data for approximately 30 s. Finally, once the worker has been hit, the underwater robot is instructed to move to its next position until the worker is hit once again. This process continues until all six points have been localized.

The continuous ground-truth trajectory, along with the six Sunflower locations, are plotted in Figure 17. The average 3D localization error across all six points was 8.98 cm, with a standard
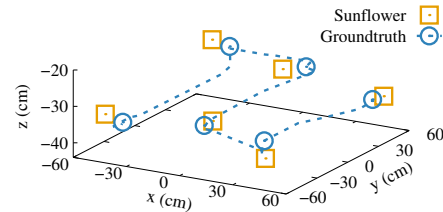
deviation of 2.03 cm. Throughout the experiment, the pool had an illuminance between 5000 lx and 23,000 lx and waves up to 10 cm high. Once driven to a specific location, the drone had an angular instability of roughly 1°/s and the underwater robot had an angular instability of 1.2°/s. Despite these real world conditions – including mobility, vibrations, sunlight, and waves – our system remains fully capable of centimeter-level 3D localization accuracy. We discuss methods to improve the speed of our tracking in §6.

5.4 Practical Factors

We next evaluate the robustness of our system to common practical factors and its overall power consumption.

Wave Conditions. Since it is impractical to physically generate and recreate waves with predefined parameters, we investigate the impact of wave dynamics on our localization accuracy with a theoretical analysis. As stated in §3.4, wave dynamics will cause an offset between the measured height to the drone/depth to the underwater robot and the *desired* distance to the incident point on the water. Specifically, the amplitude of the wave directly influences the localization error while the wavelength and frequency of the wave determines the rate at which the highest error occurs.

In our theoretical analysis, we vary the peak-to-peak wave amplitude to simulate the impact of our range offset. At each wave amplitude, we compute the localization error from all possible incident angles (0° to 55°) and average the errors. As shown in Figure 15(a), the localization errors are all below 10 cm when the peak-to-peak amplitude is smaller than 0.2 meter (a value typical for lakes [30, 36]). With larger amplitudes of 0.5 m, the localization errors caused by the range offset are still below 20 cm. Notably, this error is independent of the actual height of the drone and depth of the worker. We discuss how to remove this systematic error in §6.

Ambient Light. We next evaluate the impact of different ambient light conditions on both the queen and worker. We fix the distance between the queen and worker to 1 m in the air and illuminate each component separately with a white LED (generated from a 490 nm LED plus yellow phosphor), thus allowing us to evaluate the impact of various intensities. First, we illuminate the queen and measure our packet success rate. As shown in Figure 15(b), the queen is able to achieve a >99% packet success rate above 10 klx (corresponding to a sunny day). This demonstrates that our optical design is robust to strong ambient light, benefiting from the narrow spectral filtering of the queen's bandpass filter which is tuned to its laser's wavelength.

Next, we place the LED at 50° relative to the worker and connect our queen with a 5° incident angle. We attach the worker to

---

[2]These positions were chosen given the large size of the underwater robot and physical constraints of the pool.

Table 1: Power consumption of the queen and worker.

Queen	Power (mW)	Worker	Power (mW)
MCU	500	MCU	500
MEMS Mirror	500	AoA Sensing	528
SiPM Array	150	LC Driver	700
ADC	20	LC Shutter (On)	450
Laser + Driver	975		
Queen Total	**2145**	**Worker Total**	**2178**

a Thorlabs rotational platform [13] and rotate it from 0° to 50°, comparing the AoA results with the readings from the rotational platform. Figure 15(b) shows that the derived AoA errors are within 2° up until the light intensity is increased to 6220 lx (a moderately sunny day). Above 10 klx, the AoA error is 7.7°. The reason for this error is that the LED point source causes a second blob to appear on image sensor, causing the center point to deviate. To confirm, we removed the LED and placed the worker in the sun on an average sunny day (20,000 lx), which resulted in 2.8 °AoA error. The queen's packet success rate is not susceptible to this type of error, and had a packet success rate of 98.5% at 25,000 lx which follows the trend of Figure 15(b). It is worth noting that even if the brightness on the water's surface is above 10,000 lx, attenuation and scattering *through* the water's surface will decrease the effective illuminance – and therefore AoA error – at the worker. Furthermore, the AoA error can be further reduced by employing a bandpass filter with sufficient angular range or more robust image processing methods.

Power Consumption. Finally we examine the power consumption of the queen and worker (Table 1). Overall, each component consumes roughly 2W. Comparing to the commercially-available systems which consume around 27 W [29], our system consumes 84% less power at only 4.3 W. Furthermore, various components can be optimized to reduce the overall system power. For example, low-power MCUs can be utilized if a 600 MHz clock rate is not essential for the application scenario. Additionally, efficient laser-driver circuits can be implemented and higher-power laser diodes (which are intrinsically more power efficient than low-power diodes) can be used. On the worker, a low-power image sensor/processor can replace the OpenMV that is currently utilized. Finally, alternatives to the LC driver/shutter can be considered, such as free-space electro-optic modulators [37] which can also alter the laser's polarization.

6 DISCUSSION

Expanding Sensing Range. Although the current performance is sufficient to explore shallow-water regions that are important to study given their inaccessibility to vessels [58], more studies are required to expand the sensing range and enable exploration of deeper regions. Various optical elements can be tuned to achieve this expansion. First, decreasing the divergence of the queen's laser light would significantly lower the energy loss over distance. As shown in Figure 18(a), fixing the optical power to 80 mW and decreasing the half 3dB-divergence angle from 20 mrad (our current value) to 1 mrad (a value commonly used in high-speed FSO links [48]) increases the sensing range to 50 m. Although this requires precise adjustments to the optical elements, as well as potentially alternative beam steering techniques, prior work has demonstrated underwater transmission distances up to 21 m [38] using collimated light. If the divergence cannot be further tuned, increasing
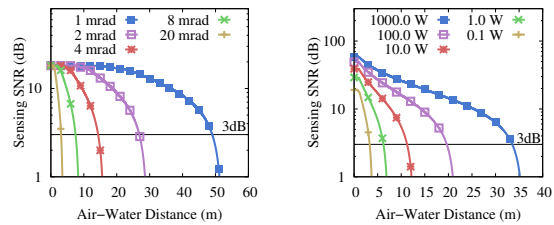
(a) Beam divergence (80 mW laser). (b) Optical power (20 mrad div.).

Figure 18: Impact of laser optical power and beam divergence on sensing range.

the aperture size of the retroreflector and fiber sensing ring will also increase the sensing SNR. Second, as shown in Figure 18(b), the optical power of the laser diode can be increased from 10s of milliwatts into the kilowatts range [56], increasing the range from 10s to 100s of meters. Notably, if the optical power of the laser diode increases, optics with sufficient damage thresholds must also be chosen. Regardless, tuning these optical parameters improves the generalizability of the system to various real-world applications.

Proactive Wave Sensing. The major source of localization error in the presence of large-amplitude waves is a single, one-dimensional height measurement in the air and underwater. Since this measurement can be out of phase with the water wave at the incident point on the surface, the resulting geometry will have an offset. One potential solution is to employ an array of ultrasonic distance sensors, as proposed by [36], to model the wave in real time. Another option is to reduce the size of the ultrasonic array and leverage historical data of ultrasonic readings. Specifically, one ultrasonic sensor could be used to estimate the wave amplitude and frequency within a sufficiently small time window. Adding another ultrasonic sensor at a known spatial location would then allow the speed of the wave to be established, providing a snapshot of the wave at any given point in time.

Continuous Robot Tracking. Although the current Sunflower implementation can support discrete tracking of an underwater robot, continuous tracking requires algorithmic and hardware improvement. Although prior work [53, 65–69] has used MEMS mirrors and laser light for fast, single-medium tracking, these algorithms do not apply to our system for the following reasons: (1) the proposed control algorithm requires zero delay between scan points, thus precluding data from being sent between scanning intervals; (2) using intensity based tracking methods is prone to false-triggers, especially in the context of the air-water interface where specular and diffusive reflections could easily trigger the scanning algorithm; (3) the system's steering and sensing FOV is limited to only ±20°, which limits the mobility of the aerial drone and underwater robot. Algorithmically, historical sensing data could be utilized by the queen to predict the underwater robot's next position based on movement continuity. Subsequent scans could then focus on the sector in the predicted direction to speed up tracking. As for hardware improvements, optical beam steering needs microradian adjustments at fast rates to cover an entire scanning region before the robot moves too far away. Furthermore, the queen and worker can use higher FSK frequencies to shorten the FFT window. Finally,

the tracking speed can also benefit from faster communication of the backscatter channel, which is currently limited by millisecond rise/fall times of off-the-shelf LC shutters. Free-space electro-optic modulators can instead be utilized to alter the polarization state of light at rates up to tens of GHz [37].

Path Blockage Avoidance. Light-based sensing and communication requires line-of-sight propagation. Any opaque objects (e.g., suspended sediment) along the path will block light signals, causing the link to become unavailable. However, since a dynamic water surface might refract the laser beam differently depending on the incident point, alternative beam paths may exist that avoid the blockage. These alternative paths would need to be tested quickly, requiring the above improvements to scanning/sensing speed. Furthermore, aerial drones and underwater robots can exploit their mobility to avoid blockages by moving probabilistically if the connection is lost for a certain amount of time.

Tracking Multiple Robots. Expanding on our bee analogy, we plan to improve the scalability of our system by allowing the queen to track multiple underwater workers. The FSK modulation of the backscatter communication can be easily leveraged to support multiple underwater workers. Specifically, a unique set of frequencies can be assigned to individual workers, allowing the queen to determine the worker's identity while decoding backscattered signals.

Integrating Downlink Communication. Although communication is currently unidirectional, the queen's laser beam can be modulated to provide data to the underwater worker. To demodulate the queen's data, the worker can collocate a photodiode with its AoA sensor. Finally, the worker can continue to modulate the backscattered signal with FSK, allowing the queen to separate its original amplitude modulation from the worker's orthogonal frequency modulation.

7 RELATED WORK

Remote Underwater Imaging. Underwater imaging has been explored for many years [39, 40, 43, 45, 81]. A recent work [45] has proposed using the photoacoustic effect to wirelessly map underwater objects. They leverage a kilowatt laser modulated at the desired acoustic frequency to generate acoustic waves below the water's surface. The induced acoustic waves bounce off objects in the water and reflect back to the surface, transmitting through the air-water interface with a 65 dB loss. A custom manufactured, extremely high-sensitivity receiver in the air then captures the weak acoustic echo. Despite the ability for 2D underwater imaging, the proposed rationale has not demonstrated the ability to handle water waves. Furthermore, the evaluated sensing range presented in [45] is very limited, only achieving 10 cm ranges in the air and 13 cm ranges underwater. NASA recently proposed a fluid lensing based underwater imaging [40] algorithm for exploring ocean worlds, which is the first remote sensing technology capable of imaging through ocean waves without distortions at sub-cm resolutions. Although promising, this approach has not demonstrated 3D *localization* of underwater objects. In comparison to our system, Sunflower is capable of locating underwater robots with a low-power laser (i.e., 10s of mW) at meter-level distances, and can be further scaled to support sensing and communication at hundreds of meters.

Underwater Robot Sensing. Underwater robot sensing techniques have been well studied in the purely underwater setting. Underwater robot localization systems mainly leverage acoustic signals. A recent work [47] presented the first underwater backscatter localization system, which reflects acoustic signals in the environment to transmit unique frequency information. Then it estimates the time-of-arrival of the backscattered signals for localization. Traditional underwater positioning can be divided into three categories depending on the length of the baseline: the ultrashort baseline (USBL), the short baseline (SBL), and the long baseline (LBL) positioning systems. All those systems [41, 70, 86, 99] leverage the travel time and the phase difference between different acoustic transducers to estimate the relative positions of the underwater robot. Our system is fundamentally different than the above-mentioned systems as none of them are capable of cross-medium (air-water) sensing, as acoustic signals cannot pass through the air-water boundary.

Optical AoA Sensing. Most prior work on optical AoA sensing utilize a photodiode array: as the light radiated from a LED follows the Lambert cosine law, the received light strength changes with respect to the AoA. S. Lee et al. [60] used a circular PD array to estimate the AoA. The circular placement of photodiodes makes the received power determined only by incidence angles. The simulation results achieved a distance error ranging from 5 to 30 cm. In [34], three orthogonal photodiodes were exploited to receive modulated signals with different frequency channels. Their simulation results showed a 5 cm positioning error. To support mobility and reduce the number of photodiodes, other work [94–96] included an accelerometer. When photodiodes were rotated to different orientations sensed by the accelerometer, the received power corresponding to these orientations was measured.

8 CONCLUSION

We presented Sunflower, the first-of-its-kind system for demonstrating direct air-water 3D localization using laser light between an aerial drone and an underwater robot. The implemented prototypes are built with off-the-shelf elements and customized PCBs. Real-world experiments showed the robustness and accuracy of Sunflower in the presence of waves, making Sunflower a foundational technology for locating underwater robots from the air and enabling autonomous aquatic applications.

REFERENCES

[1] 2021. AD7895. https://www.analog.com/media/en/technical-documentation/data-sheets/ad7895.pdf.
[2] 2021. ADuM1250. https://www.analog.com/media/en/technical-documentation/data-sheets/ADUM1250_1251.pdf.

[3] 2021. ADuM210. https://www.digikey.com/en/products/base-product/analog-devices-inc/505/ADUM210/116860.

[4] 2021. Archimedes' Spiral. https://mathworld.wolfram.com/ArchimedesSpiral.html.

[5] 2021. ARRAYJ-30035-16P-PCB. https://www.analog.com/media/en/technical-documentation/data-sheets/ad7895.pdf.

[6] 2021. C140TMD-A. https://www.thorlabs.com/thorproduct.cfm?partnumber=C140TMD-A.

[7] 2021. C440TMD-A. https://www.gophotonics.com/products/optical-lenses/thorlabs-inc/33-46-c440tmd-a.

[8] 2021. Edmund Optics 39-02. https://www.edmundoptics.com/p/127mm-dia-340-560nm-4-achromatic-waveplate/39586/.

[9] 2021. Edmund Optics 58-840. https://www.edmundoptics.com/p/f20-visible-22mm-heo-series-m12-mu-videotrade-imaging-lens/15638/.

[10] 2021. Electromagnetic absorption by water. https://en.wikipedia.org/wiki/Electromagnetic_absorption_by_water.

[11] 2021. EXACTD-362 Angle-of-Arrival Photodiode Module. https://www.excelitas.com/product/exactd-362-angle-arrival-photodiode-module.

[12] 2021. FBH450-10. https://www.thorlabs.com/thorproduct.cfm?partnumber=FBH450-10.

[13] 2021. LC1A. https://www.thorlabs.com/thorproduct.cfm?partnumber=LC1A/M.

[14] 2021. LM2577. https://www.ti.com/product/LM2577.

[15] 2021. LT1615. https://www.analog.com/en/products/lt1615.html.

[16] 2021. MCP45HV51. https://www.microchip.com/en-us/product/MCP45HV51.

[17] 2021. MicroPython libraries. https://docs.micropython.org/en/latest/library/index.html.

[18] 2021. Mirrorcle A7B2.3-3600AL-TINY48.4- A/F/EP. https://www.mirrorcletech.com/pdf/Mirrorcle_MEMS_Packages_and_Mounts_-_User_Guide.pdf.

[19] 2021. OPA340. https://www.ti.com/product/OPA340.

[20] 2021. OpenMV Cam H7. https://openmv.io/collections/products/products/openmv-cam-h7-plus.

[21] 2021. OPT101 Monolithic Photodiode and Single-Supply Transimpedance Amplifier. https://www.ti.com/lit/ds/symlink/opt101.pdf.

[22] 2021. Optical Grade Fiber Optics. https://www.edmundoptics.com/f/optical-grade-fiber-optics/11460/.

[23] 2021. PFSQ05-03-G01. https://www.thorlabs.com/thorproduct.cfm?partnumber=PFSQ05-03-G01.

[24] 2021. Refractometer. https://en.wikipedia.org/wiki/Refractometer.

[25] 2021. Snell's law. https://en.wikipedia.org/wiki/Snell%27s_law.

[26] 2021. Thorlabs PAX1000VIS polarimeter. https://www.thorlabs.com/newgrouppage9.cfm?objectgroup_id=1564.

[27] 2021. TIR Retroreflector Prisms. https://www.thorlabs.com/newgrouppage9.cfm?objectgroup_id=145.

[28] 2021. TRH127-020-A-ML. https://www.thorlabs.com/thorproduct.cfm?partnumber=TRH127-020-A-ML.

[29] 2021. UNDERWATER GPS G2. http://store.waterlinked.com/wp-content/uploads/2020/09/W-MK-20010-1_Underwater_GPS_G2_Datasheet.pdf.

[30] 2021. Wind wave. https://en.wikipedia.org/wiki/Wind_wave.

[31] 2022. Bolder Vision Optik Pi-cell Liquid Crystal Shutter. https://boldervision.com/product/pi-cell-liquid-crystal-shutter/.

[32] 2022. Sunflower Demo Video. https://youtu.be/ofpqm2G2s_U.

[33] Alex Alcocer, Paulo Oliveira, and Antonio Pascoal. 2006. Underwater acoustic positioning systems based on buoys with GPS. In Proceedings of the Eighth European Conference on Underwater Acoustics, Vol. 8. 1–8.

[34] Ahmed Arafa, Sumant Dalmiya, Richard Klukas, and Jonathan F Holzman. 2015. Angle-of-arrival reception for optical wireless location technology. Optics Express 23, 6 (2015), 7755. https://doi.org/10.1364/oe.23.007755

[35] Joseph Ayers, Jan Witting, Cricket Wilbur, Paul M. Zavracky, Nicol E. McGruer, and Donald P. Massa. 2000. Biomimetic Robots for Shallow Water Mine Countermeasures 1.

[36] Charles J. Carver, Zhao Tian, Hongyong Zhang, Kofi M. Odame, Alberto Quattrini Li, and Xia Zhou. 2020. AmphiLight: Direct Air-Water Communication with Laser Light. In 17th USENIX Symposium on Networked Systems Design and Implementation (NSDI 20). USENIX Association, Santa Clara, CA, 373–388. https://www.usenix.org/conference/nsdi20/presentation/carver

[37] Datong Chen, Harold R Fetterman, Antao Chen, William H Steier, Larry R Dalton, Wenshen Wang, and Yongqiang Shi. 1997. Demonstration of 110 GHz electro-optic polymer modulators. Applied Physics Letters 70, 25 (1997), 3335–3337.

[38] Yifei Chen, Meiwei Kong, Tariq Ali, Jiongliang Wang, Rohail Sarwar, Jun Han, Chaoyang Guo, Bing Sun, Ning Deng, and Jing Xu. 2017. 26 m/5.5 Gbps air-water optical wireless communication based on an OFDM-modulated 520-nm laser diode. Optics express 25, 13 (2017), 14760–14765.

[39] Ved Chirayath and Ron Instrella. 2019. Fluid lensing and machine learning for centimeter-resolution airborne assessment of coral reefs in American Samoa. Remote Sensing of Environment 235 (2019), 111475. https://doi.org/10.1016/j.rse.2019.111475

[40] Ved Chirayath and Alan Li. 2019. Next-Generation Optical Sensing Technologies for Exploring Ocean Worlds—NASA FluidCam, MiDAR, and NeMO-Net. Frontiers in Marine Science 6 (2019). https://doi.org/10.3389/fmars.2019.00521

[41] Yang Cong, Changjun Gu, Tao Zhang, and Yajun Gao. 2021. Underwater robot sensing technology: A survey. Fundamental Research 1, 3 (2021), 337–345. https://doi.org/10.1016/j.fmre.2021.03.002

[42] Peter Corke, Carrick Detweiler, Matthew Dunbabin, Michael Hamilton, Daniela Rus, and Iuliu Vasilescu. 2007. Experiments with underwater robot localization and tracking. In IEEE International Conference on Robotics and Automation (ICRA). IEEE, 4556–4561.

[43] T. Dolereit and A. Kuijper. 2014. Converting underwater imaging into imaging in air. In 2014 International Conference on Computer Vision Theory and Applications (VISAPP), Vol. 1. IEEE Computer Society, Los Alamitos, CA, USA, 96–103. https://doi.ieeecomputersociety.org/

[44] Randima Fernando. 2004. GPU Gems: Programming Techniques, Tips and Tricks for Real-Time Graphics. Pearson Higher Education.

[45] Aidan Fitzpatrick, Ajay Singhvi, and Amin Arbabian. 2020. An Airborne Sonar System for Underwater Remote Sensing and Imaging. IEEE Access 8 (2020), 189945–189959. https://doi.org/10.1109/ACCESS.2020.3031808

[46] Reza Ghaffarivardavagh, Sayed Saad Afzal, Osvy Rodriguez, and Fadel Adib. 2020. Underwater Backscatter Localization: Toward a Battery-Free Underwater GPS. In Proc. of HotNets.

[47] Reza Ghaffarivardavagh, Sayed Saad Afzal, Osvy Rodriguez, and Fadel Adib. 2020. Underwater Backscatter Localization: Toward a Battery-Free Underwater GPS. In Proceedings of the 19th ACM Workshop on Hot Topics in Networks (Virtual Event, USA) (HotNets '20). Association for Computing Machinery, New York, NY, USA, 125–131. https://doi.org/10.1145/3422604.3425950

[48] Z. Ghassemlooy, W. Popoola, and S. Rajbhandari. 2012. Optical Wireless Communications: System and Channel Modelling with MATLAB®. Taylor & Francis. https://books.google.com/books?id=jpXGCN1qVQ4C

[49] Stefan Gundacker and Arjan Heering. 2020. The silicon photomultiplier: fundamentals and applications of a modern solid-state photon detector. Physics in Medicine & Biology 65, 17 (2020), 17TR01.

[50] Linlin Guo, Lei Wang, Jialin Liu, and Wei Zhou. 2016. A survey on motion detection using WiFi signals. In 2016 12th International Conference on Mobile Ad-Hoc and Sensor Networks (MSN). IEEE, 202–206.

[51] Michael L Hawkins. 1990. A generalization of Snell's law. Technical Report. NAVAL POSTGRADUATE SCHOOL MONTEREY CA.

[52] Bharat Joshi, Sharmin Rahman, Michail Kalaitzakis, Brennan Cain, James Johnson, Marios Xanthidis, Nare Karapetyan, Alan Hernandez, Alberto Quattrini Li, Nikolaos Vitzilaios, et al. 2019. Experimental comparison of open source visual-inertial-based state estimation algorithms in the underwater domain. In IEEE/RSJ International Conference on Intelligent Robots and Systems (IROS). IEEE, 7227–7233.

[53] Abhishek Kasturi, Veljko Milanovic, Bryan H Atwood, and James Yang. 2016. UAV-borne lidar with MEMS mirror-based scanning capability. In Laser Radar Technology and Applications XXI, Vol. 9832. SPIE, 206–215.

[54] Ozkan Katircioğlu, Hasan Isel, Osman Ceylan, Firat Taraktas, and H Bulent Yagci. 2011. Comparing ray tracing, free space path loss and logarithmic distance path loss models in success of indoor localization with RSSI. In 2011 19thTelecommunications Forum (TELFOR) Proceedings of Papers. IEEE, 313–316.

[55] Hemani Kaushal and Georges Kaddoum. 2016. Underwater optical wireless communication. IEEE access 4 (2016), 1518–1547.

[56] Tobias Könning, Florian Harth, Philipp König, Paul Wolf, Michael Stoiber, Heiko Kissel, and Bernd Köhler. 2020. Kilowatt-class high power fiber-coupled diode lasers at 450nm. In High-Power Diode Laser Technology XVIII, Vol. 11262. International Society for Optics and Photonics, 112620N.

[57] Neil Harvey Kussat, C David Chadwell, and Richard Zimmerman. 2005. Absolute positioning of an autonomous underwater vehicle using GPS and acoustic measurements. IEEE Journal of Oceanic Engineering 30, 1 (2005), 153–164.

[58] Tiit Kutser, John Hedley, Claudia Giardino, Chris Roelfsema, and Vittorio E Brando. 2020. Remote sensing of shallow waters–A 50 year retrospective and future directions. Remote Sensing of Environment 240 (2020), 111619.

[59] Ulf Larsson, Johan Forsberg, and Ake Wernersson. 1996. Mobile robot localization: integrating measurements from a time-of-flight laser. IEEE Transactions on Industrial Electronics 43, 3 (1996), 422–431.

[60] Seongsu Lee and Sung-Yoon Jung. 2012. Location awareness using Angle-of-arrival based circular-PD-array for visible light communication. 2012 18th Asia-Pacific Conference on Communications (APCC) (2012). https://doi.org/10.1109/apcc.2012.6388185

[61] Samuel Lensgraf, Amy Sniffen, Zachary Zitzewitz, Evan Honnold, Jennifer Jain, Weifu Wang, Alberto Quattrini Li, and Devin Balkcom. 2021. Droplet: Towards Autonomous Underwater Assembly of Modular Structures. In Proceedings of Robotics: Science and Systems. Virtual. https://doi.org/10.15607/RSS.2021.XVII.054

[62] John J Leonard and Alexander Bahr. 2016. Autonomous underwater vehicle navigation. Springer Handbook of Ocean Engineering (2016), 341–358.

[63] Chi Lin, Yongda Yu, Jie Xiong, Yichuan Zhang, Lei Wang, Guowei Wu, and Zhongxuan Luo. 2021. Shrimp: A Robust Underwater Visible Light Communication System. In *Proceedings of the 27th Annual International Conference on Mobile Computing and Networking* (New Orleans, Louisiana) *(MobiCom '21)*. Association for Computing Machinery, New York, NY, USA, 134–146. https://doi.org/10.1145/3447993.3448616

[64] Kai Lingemann, Andreas Nüchter, Joachim Hertzberg, and Hartmut Surmann. 2005. High-speed laser localization for mobile robots. *Robotics and autonomous systems* 51, 4 (2005), 275–296.

[65] Daniel Lovell, Veljko Milanovic, Abhishek Kasturi, Frank Hu, Karan Soni, Derek Ho, Bryan H Atwood, Lj Ristic, Xiaomeng Liu, and Sanjeev J Koppal. 2022. Optical MEMS enable next generation solutions for robot vision and human-robot interaction. In *MOEMS and Miniaturized Systems XXI*, Vol. 12013. SPIE, 15–29.

[66] Veljko Milanović and Abhishek Kasturi. 2013. Real-time 3D Tracking: The system "MEMSEye" can be used for optical 3D position and orientation measurement. *Optik & Photonik* 8, 4 (2013), 55–59.

[67] Veljko Milanović, Abhishek Kasturi, James Yang, and Frank Hu. 2017. A fast single-pixel laser imager for VR/AR headset tracking. In *MOEMS and Miniaturized Systems XVI*, Vol. 10116. International Society for Optics and Photonics, 101160E.

[68] Veljko Milanovic and Wing Kin Lo. 2008. Fast and high-precision 3D tracking and position measurement with MEMS micromirrors. In *2008 IEEE/LEOS International Conference on Optical MEMs and Nanophotonics*. IEEE, 72–73.

[69] V. Milanović, N. Siu, A. Kasturi, M. Radojičić, and Y. Su. 2011. MEMSEye for optical 3D position and orientation measurement. In *MOEMS and Miniaturized Systems X*, Vol. 7930. 79300U.

[70] M. Morgado, P. Oliveira, and C. Silvestre. 2013. Tightly coupled ultrashort baseline and inertial navigation system for underwater vehicles: An experimental validation. *Journal of Field Robotics* 30, 1 (2013), 142–170. https://doi.org/10.1002/rob.21442 arXiv:https://onlinelibrary.wiley.com/doi/pdf/10.1002/rob.21442

[71] Satomi Ohata, Yu Eriguchi, and Kazuo Ishii. 2007. AquaBox Series: Small Underwater Robot Systems for Shallow Water Observation. In *2007 Symposium on Underwater Technology and Workshop on Scientific Use of Submarine Cables and Related Technologies*. 314–319. https://doi.org/10.1109/UT.2007.370796

[72] Oluseun D Oyeleke, Sadiq Thomas, Olabode Idowu-Bismark, Petrus Nzerem, and Idris Muhammad. 2020. Absorption, diffraction and free space path losses modeling for the terahertz band. *Int. J. Eng. Manuf* 10 (2020), 54.

[73] Liam Paull, Sajad Saeedi, Mae Seto, and Howard Li. 2013. AUV navigation and localization: A review. *IEEE Journal of oceanic engineering* 39, 1 (2013), 131–149.

[74] D Howell Peregrine. 1976. Interaction of water waves and currents. *Advances in applied mechanics* 16 (1976), 9–117.

[75] JA Pérez, José A Castellanos, JMM Montiel, Jose Neira, and Juan D Tardos. 1999. Continuous mobile robot localization: Vision vs. laser. In *Proceedings 1999 IEEE International Conference on Robotics and Automation (Cat. No. 99CH36288C)*, Vol. 4. IEEE, 2917–2923.

[76] William Wesley Peterson, Wesley Peterson, Edward J Weldon, and Edward J Weldon. 1972. Error-correcting codes. (1972).

[77] Yiming Qian, Yinqiang Zheng, Minglun Gong, and Yee-Hong Yang. 2018. Simultaneous 3D Reconstruction for Water Surface and Underwater Scene. In *Proceedings of the European Conference on Computer Vision (ECCV)*.

[78] John Rzasa. 2012. *Pointing, acquisition, and tracking for directional wireless communications networks*. Ph. D. Dissertation.

[79] Norimitsu Sakagami, Mizuho Shibata, Sadao Kawamura, Toshifumi Inoue, Hiroyuki Onishi, and Shigeo Murakami. 2010. An attitude control system for underwater vehicle-manipulator systems. In *2010 IEEE International Conference on Robotics and Automation*. 1761–1767. https://doi.org/10.1109/ROBOT.2010.5509800

[80] Florian Shkurti, Anqi Xu, Malika Meghjani, Juan Camilo Gamboa Higuera, Yogesh Girdhar, Philippe Giguere, Bir Bikram Dey, Jimmy Li, Arnold Kalmbach, Chris Prahacs, et al. 2012. Multi-domain monitoring of marine environments using a heterogeneous robot team. In *2012 IEEE/RSJ International Conference on Intelligent Robots and Systems*. IEEE, 1747–1753.

[81] Ajay Singhvi, Aidan Fitzpatrick, and Amin Arbabian. 2020. Resolution Enhanced Non-Contact Thermoacoustic Imaging using Coded Pulse Excitation. In *2020 IEEE International Ultrasonics Symposium (IUS)*. 1–4. https://doi.org/10.1109/IUS46767.2020.9251350

[82] PB Sujit, Joao Sousa, and F Lobo Pereira. 2009. UAV and AUVs coordination for ocean exploration. In *Oceans 2009-Europe*. IEEE, 1–7.

[83] Li Sun, Souvik Sen, Dimitrios Koutsonikolas, and Kyu-Han Kim. 2015. Widraw: Enabling hands-free drawing in the air on commodity wifi devices. In *Proceedings of the 21st Annual International Conference on Mobile Computing and Networking*. 77–89.

[84] Gunnar Taraldsen, Tor Arne Reinen, and Tone Berg. 2011. The underwater GPS problem. In *OCEANS 2011 IEEE-Spain*. IEEE, 1–8.

[85] Blair Thornton, Tamaki Ura, Yoshiaki Nose, and Stephen Turnock. 2007. Zero-G Class Underwater Robots: Unrestricted Attitude Control Using Control Moment Gyros. *IEEE Journal of Oceanic Engineering* 32, 3 (2007), 565–583. https://doi.org/10.1109/JOE.2007.899274

[86] Antonio Vasilijevic, Bruno Borovic, and Zoran Vukić. 2012. Underwater Vehicle Localization with Complementary Filter: Performance Analysis in the Shallow Water Environment. *Journal of Intelligent & Robotic Systems* 68 (12 2012). https://doi.org/10.1007/s10846-012-9766-6

[87] Lloyd Butler VK5BR. 1987. Underwater radio communication. *Originally published in Amateur Radio* (1987).

[88] Kyle L Walker, Adam A Stokes, Aristides Kiprakis, and Francesco Giorgio-Serchi. 2020. Impact of thruster dynamics on the feasibility of ROV station keeping in waves. In *Global Oceans 2020: Singapore–US Gulf Coast*. IEEE, 1–7.

[89] E. Westman and M. Kaess. 2018. *Underwater AprilTag SLAM and Calibration for High Precision Robot Localization*. Technical Report CMU-RI-TR-18-43. Robotics Institute, Carnegie Mellon University.

[90] Dan Wu, Ruiyang Gao, Youwei Zeng, Jinyi Liu, Leye Wang, Tao Gu, and Daqing Zhang. 2020. FingerDraw: Sub-wavelength level finger motion tracking with WiFi signals. *Proceedings of the ACM on Interactive, Mobile, Wearable and Ubiquitous Technologies* 4, 1 (2020), 1–27.

[91] Yue Wu, Purui Wang, Kenuo Xu, Lilei Feng, and Chenren Xu. 2020. Turboboosting visible light backscatter communication. In *Proceedings of the Annual conference of the ACM Special Interest Group on Data Communication on the applications, technologies, architectures, and protocols for computer communication*. 186–197.

[92] Xieyang Xu, Yang Shen, Junrui Yang, Chenren Xu, Guobin Shen, Guojun Chen, and Yunzhe Ni. 2017. Passivevlc: Enabling practical visible light backscatter communication for battery-free iot applications. In *Proceedings of the 23rd Annual International Conference on Mobile Computing and Networking*. 180–192.

[93] Bohuan Xue, Jianhao Jiao, Yilong Zhu, Linwei Zhen, Dong Han, Ming Liu, and Rui Fan. 2019. Automatic calibration of dual-LiDARs using two poles stickered with retro-reflective tape. In *2019 IEEE International Conference on Imaging Systems and Techniques (IST)*. IEEE, 1–6.

[94] M. Yasir, S. Ho, and B. N. Vellambi. 2014. Indoor Positioning System Using Visible Light and Accelerometer. *Journal of Lightwave Technology* 32, 19 (2014), 3306–3316.

[95] M. Yasir, S. Ho, and B. N. Vellambi. 2016. Indoor Position Tracking Using Multiple Optical Receivers. *Journal of Lightwave Technology* 34, 4 (2016), 1166–1176.

[96] Muhammad Yasir, Siu-Wai Ho, and Badri N Vellambi. 2013. Indoor localization using visible light and accelerometer. In *2013 IEEE global communications conference (GLOBECOM)*. IEEE, 3341–3346.

[97] Junku Yuh, Giacomo Marani, and D Richard Blidberg. 2011. Applications of marine robotic vehicles. *Intelligent service robotics* 4, 4 (2011), 221–231.

[98] Jisu Yun and Byung-Jun Jang. 2016. Ambient light backscatter communication for IoT applications. *Journal of electromagnetic Engineering and Science* 16, 4 (2016), 214–218.

[99] Zhai Yuyi, Gong Zhenbang, Wang Lei, Zhang Ruiyong, and Luo Huanxin. 2009. Study of Underwater Positioning Based on Short Baseline Sonar System. In *2009 International Conference on Artificial Intelligence and Computational Intelligence*, Vol. 2. 343–346. https://doi.org/10.1109/AICI.2009.83